



Label-free brain tumor imaging using Raman-based methods

Todd Hollon¹ · Daniel A. Orringer²

Received: 16 December 2019 / Accepted: 20 December 2019
© Springer Science+Business Media, LLC, part of Springer Nature 2020

Abstract

Introduction Label-free Raman-based imaging techniques create the possibility of bringing chemical and histologic data into the operation room. Relying on the intrinsic biochemical properties of tissues to generate image contrast and optical tissue sectioning, Raman-based imaging methods can be used to detect microscopic tumor infiltration and diagnose brain tumor subtypes.

Methods Here, we review the application of three Raman-based imaging methods to neurosurgical oncology: Raman spectroscopy, coherent anti-Stokes Raman scattering (CARS) microscopy, and stimulated Raman histology (SRH).

Results Raman spectroscopy allows for chemical characterization of tissue and can differentiate normal and tumor-infiltrated tissue based on variations in macromolecule content, both *ex vivo* and *in vivo*. To improve signal-to-noise ratio compared to conventional Raman spectroscopy, a second pulsed excitation laser can be used to coherently drive the vibrational frequency of specific Raman active chemical bonds (i.e. symmetric stretching of $-CH_2$ bonds). Coherent Raman imaging, including CARS and stimulated Raman scattering microscopy, has been shown to detect microscopic brain tumor infiltration in fresh brain tumor specimens with submicron image resolution. Advances in fiber-laser technology have allowed for the development of intraoperative SRH as well as artificial intelligence algorithms to facilitate interpretation of SRH images. With molecular diagnostics becoming an essential part of brain tumor classification, preliminary studies have demonstrated that Raman-based methods can be used to diagnose glioma molecular classes intraoperatively.

Conclusions These results demonstrate how label-free Raman-based imaging methods can be used to improve the management of brain tumor patients by detecting tumor infiltration, guiding tumor biopsy/resection, and providing images for histopathologic and molecular diagnosis.

Keywords Stimulated Raman histology · Raman spectroscopy · Coherent Raman imaging · Stimulated Raman scattering microscopy · Coherent anti-Stokes Raman scattering microscopy · Label-free imaging · Intraoperative pathology · Molecular imaging

Introduction

Image guidance is essential for providing safe and effective neurosurgical care for brain tumor patients. Frameless navigation, fluorescence-guided surgery, and intraoperative structural imaging, including computed tomography and magnetic resonance imaging, has resulted in improved extent of resection and patient outcomes [1–3]. While these methods are indispensable in modern neurosurgical oncology, they are limited by the need for contrast agents (e.g.

gadolinium) or fluorescent dyes (e.g. 5-aminolevulinic acid) to label tumor infiltration. The limitations of current techniques include (1) false negative labelling in primary diffuse lower grade and malignant gliomas and (2) false positive labelling in recurrent gliomas or pseudoprogression/treatment effect, leading to postoperative residual tumor burden or resection of non-tumor infiltrated brain tissue, respectively [4].

MRI-based methods and fluorescence-guided surgery also fail to resolve tumor infiltration on a microscopic scale. Given the challenge that exists in differentiating tumor from non-infiltrated brain innovations in imaging are required to eliminate uncertainty during brain tumor resection, enabling safer and more complete operations.

✉ Daniel A. Orringer
Daniel.Orringer@nyulangone.org

¹ University of Michigan, Ann Arbor, USA

² New York University, New York, NY, USA

Label-free techniques have been developed that directly detect tumor infiltration based on the biomolecular properties of the tissue and, in some cases, with sub-micron resolution. Vibrational spectroscopy, which includes infrared and Raman spectroscopy, is a label-free technique proposed for use in neurosurgery since at least since 1990 [5]. The advantage of using Raman-based methods in neurosurgical oncology is that the Raman spectra represents the vibrational fingerprint of a surgical specimen; this fingerprint provides quantitative biochemical information regarding its molecular composition. Over the previous decade, Raman-based methods have been studied as a means of improving the diagnostic yield of stereotactic brain tumor biopsies [6], in vivo detection of tumor infiltration [7], intraoperative histopathologic diagnosis [8], and molecular classification [9]. Here, we discuss several Raman-based spectroscopic and imaging methods that have been proposed for clinical use including spontaneous Raman spectroscopy, coherent anti-Stokes Raman scattering microscopy (CARS). We also explore the use of stimulated Raman histology (SRH) which is undergoing expanding adoption for clinical use during brain tumor surgery.

Raman spectroscopy

Overview

Elastic photon scattering, or Rayleigh scattering, occurs when the wavelength of the incident photon is the same as the scattered photon after interacting with a material or biomedical specimen. In the visible spectrum, between 380 and 750 nm wavelength, the majority of photons are scattered elastically. However, a small percentage of photons (1:10 million) undergo *inelastic* scattering and change wavelength by either absorbing from or losing energy to the incident material. The change in the wavelength that results from inelastic scattering is called Raman effect, discovered in 1928 and was awarded the Nobel Prize [10]. The Raman effect is weak relative to Rayleigh scattering; however, using narrow-band laser excitation and sensitive spectrometers, Raman scattering can be detected and measured to generate spectra from the indecent tissue.

Raman spectroscopy has multiple applications in biomedicine due to its ability to characterize individual molecules and biological tissues. Raman spectral peaks correspond to specific vibrational modes of chemical bonds, such as stretching, bending, or scissoring. The $-\text{CH}_2$ symmetric stretching mode, for example, plays an essential role in characterizing biomedical specimens using Raman spectroscopy due to the high concentration of fatty acids. The specificity of Raman spectroscopy can therefore be used to quantify the chemical composition of biological tissues. The vibrational

fingerprint of biological tissues is a product of its composition of macromolecules (i.e. nucleic acids, proteins, and lipids) and the sum of the vibrational spectra of the tissue constituents.

Spontaneous Raman spectroscopy

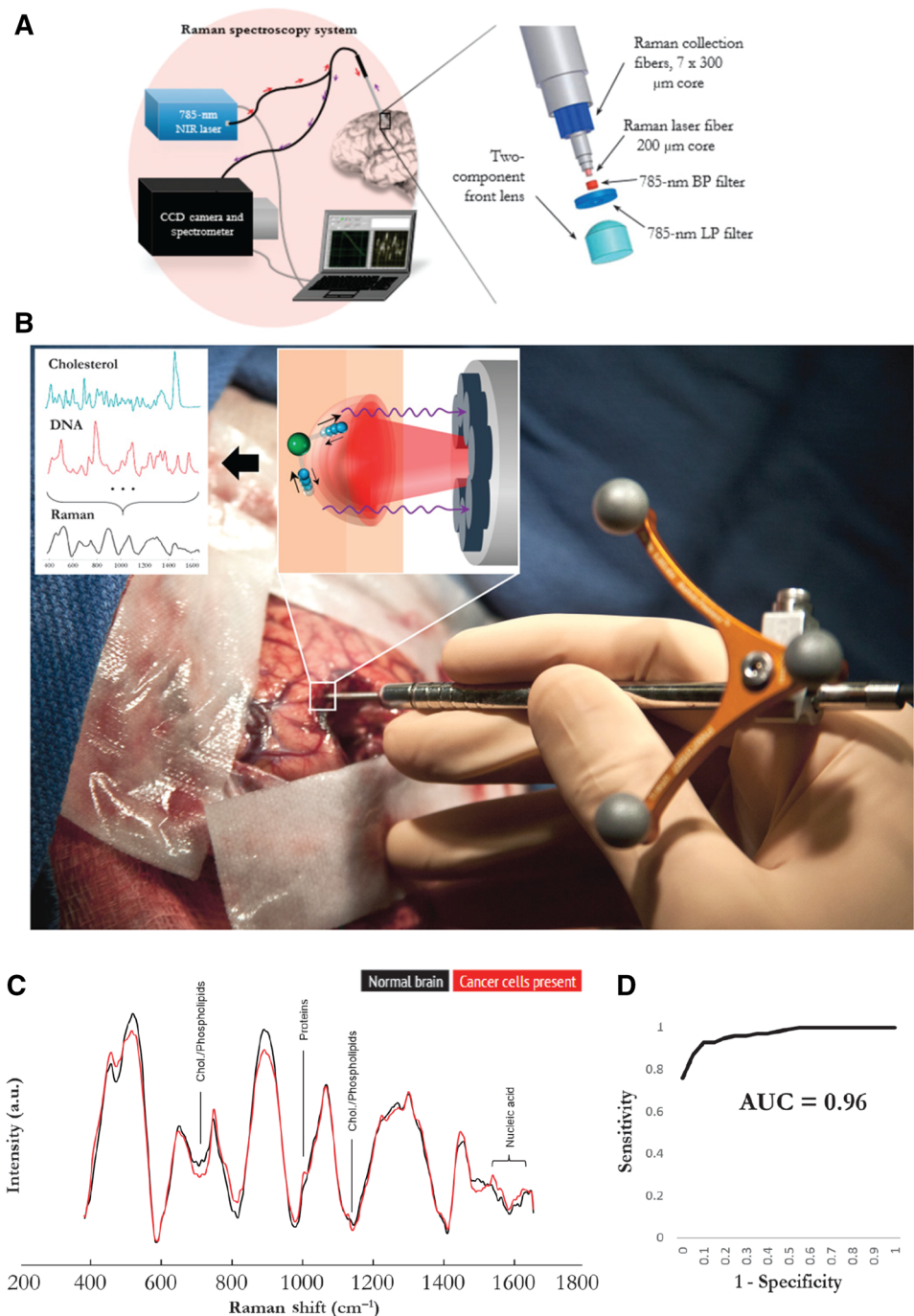
Spontaneous Raman spectroscopy was used in 1990 to characterize brain tissue and involved distinguishing normal versus edematous brain [11]. A strong 3390 cm^{-1} Raman peak corresponding to the O–H stretching mode was found in edematous brain, known to have higher water content. Krafft et al. performed several influential early studies on the use of Raman spectroscopy in neurosurgical oncology [12, 13]. The group were able to differentiate glioblastoma tissue from healthy brain tissue using lipid and water content after performing a detailed spectral analysis of 12 major brain lipids. The same investigators performed a landmark proof-of-concept study employing Raman spectroscopy to detect intracerebral tumors in vivo by brain surface mapping [14]. In a murine metastatic brain tumor model, Raman spectroscopy covering $3.6 \times 3.2\text{ mm}$ of cortical surface detected melanotic tumors in mouse brain. The Raman spectra of the metastatic tumors displayed additional Raman shifts near $597, 976, 1404,$ and 1.595 cm^{-1} due to spectral contribution of the melanin pigment.

Intraoperative brain tumor biopsy guidance was an early use case for clinical Raman spectroscopy. Identifying regions of viable tumor and avoid necrotic tissue in malignant glioma increases the diagnostic yield of biopsy specimens. Necrotic specimens contain a prominent Raman peak at 1739 cm^{-1} , demonstrating significantly higher concentration of cholesterol and cholesteryl esters [15]. Using linear discriminant analysis on spectral data from biopsy specimens, accuracy for differentiating necrotic versus viable tumor approaches 100%. Kalkanis et al. were able to differentiate normal brain, necrosis and viable glioblastoma tissue in frozen brain tumor sections with an accuracy of 97.8% [6]. In a follow up study, five frozen sections (normal, necrosis, dense glioblastoma, two infiltrating glioblastoma) were mapped at five Raman shift wavenumbers across the entire specimen in $300\text{ }\mu\text{m}$ square step sizes [16]. Tissue maps were able to identify interfaces between grey and white matter, necrosis, glioblastoma, and infiltrating tumor. Three key Raman spectral regions were used to generate a virtual RGB color scheme [17]. Red (1004 cm^{-1} channel), green ($1300:1344\text{ cm}^{-1}$ channel), and blue (1600 cm^{-1} channel) color scales were assigned to Raman peak intensities and fused for multichannel imaging. The multichannel color maps could discriminate white matter, gray matter, and tumor tissue with diagnostic accuracy of approximately 90% on a cross-validation.

A Raman spectroscopy probe system for in vivo intraoperative brain tissue classification has been developed due to recent advances in fiber-laser-based technology (Fig. 1) [18]. A handheld fiber-optic probe was placed in direct contact with the brain in the resection cavities of 17 patients with gliomas (low- and high-grade) [7]. Time to image acquisition was 0.2 s for each area interrogated and measured 0.5 mm in diameter; sampling depth of the probe was 1 mm. Using a boosted tree algorithm to classify intraoperative Raman spectra, the investigators were able to

distinguish normal brain from tumor-invaded brain (> 15% tumor cell invasion) with an accuracy of 92% (sensitivity = 93%, specificity = 91%). Both low- and high-grade gliomas were detected with similar accuracy. Similar methods were used to identify glioma cell infiltration several centimeters beyond radiographically abnormal regions on MRI [19, 20]. These results represent a promising step forward towards translating Raman spectroscopy to intraoperative use and brain tumor resection guidance [21].

Fig. 1 In vivo intraoperative Raman spectroscopy. **a** Experimental setup diagram with the 785 nm NIR laser and the high-resolution charge-coupled device spectroscopic detector used with the Raman fiber optic probe. The core material was fused silica. *BP* band-pass, *LP* long-pass. **b** The handheld contact fiber optic probe for Raman spectroscopy. The probe (Emvision, LLC) was used to interrogate brain tissue during surgery. A schematic diagram illustrates the excitation of different molecular species, such as cholesterol and DNA, to produce the Raman spectra of cancer versus normal brain tissue. The spectral differences occur owing to the vibrational modes of various molecular species. A simple molecular vibrational mode is conceptually depicted (individual atoms in blue and green) interacting with the laser light (in red) to produce Raman scattering (in purple). **c** Raman spectra for discrimination of cancer tissue. Average Raman spectra of in vivo measurements for normal brain (all 66 spectra averaged) and tissue containing glioma cancer cells (all 95 spectra averaged). The corresponding molecular contributors are identified for the most significant differences between the spectra for normal and cancer tissues. Chol., cholesterol. **d** Receiver operating characteristic (ROC) curve analysis of in vivo detection of glioma based on Raman spectroscopy. This was generated using the boosted trees classification method. AUC, area under the curve. Figure and Caption adapted from Figs. 1 and 3 from [7]



Coherent Raman scattering microscopy

A limitation of spontaneous Raman scattering is poor signal-to-noise ratio; with only a small percentage of incident photons (10^8) are scattered inelastically, long acquisition times are needed to produce reliable spectra for biomedical specimen analysis. Additionally, no spatial information about the specimen is available because time constraints limit the acquisition of Raman spectra to a single spatial region. Coherent Raman scattering (CRS) microscopy was developed to improve the signal-to-noise ratio, reduce spectral acquisition time, and produce histologic images with subcellular spatial resolution. Rather than obtaining a broadband Raman spectra across a range of Raman shift wavenumbers ($0\text{--}3500\text{ cm}^{-1}$), CRS increases signal intensity by targeting a specific (narrowband) wavenumber using a second pulsed excitation laser beam to coherently drive the vibrational frequency of Raman active chemical bonds. CRS microscopy can produce histologic images of biological tissues because the Raman signal is several orders of magnitude greater ($> 10,000$ -fold) than that of spontaneous Raman scattering. Image contrast is generated without the need for labels or dyes because the Raman effect results from the biochemical composition of tissues. Label-free CRS microscopy eliminates the need for extensive tissue preparation, making the technique an ideal imaging modality for intraoperative brain tumor specimens. The two major methods of CRS microscopy applied to brain tumor imaging are coherent anti-Stokes scattering microscopy (CARS) and stimulated Raman histology (SRH).

Coherent anti-Stokes Raman stimulated (CARS) microscopy

Evans et al. used CARS microscopy to image fresh unfixed and unstained *ex vivo* samples from an orthotopic human astrocytoma mouse model [22, 23]. High-resolution mosaic images of a mouse brain were obtained using $700 \times 700\ \mu\text{m}$ fields of view. Histologic features shown in CARS images were comparable to standard hematoxylin and eosin (H&E) histology. Depending on tissue type and wavelength, imaging depth ranged from $25\text{--}80\ \mu\text{m}$. CARS microscopy was capable of producing chemically selective images of lipid (2845 cm^{-1} , CH_2 symmetric stretching) and proteins (CH_3 stretch, 2920 cm^{-1} ; amide I vibration, 2960 cm^{-1}) within samples. The chemical selectivity of CARS imaging allowed for brain-tumor margin delineation in the mouse model. Another investigation used CARS imaging to probe C–H molecular vibrations in different cryosectioned brain tumors (glioblastoma, melanoma and

breast cancer metastasis) to assess lipid content compared to normal brain tissue [24]. All tumor types were found to have a lower lipid CARS signal intensity than normal parenchyma, reflecting decreased lipid/protein ratio within malignant tissues. The morphochemical contrast between normal brain and tumor enabled CARS images to delineate tumor tissue irrespective of tumor type. The same group of investigators used a fluorescent label (5-aminolevulinic acid) to confirm that CARS microscopy could identify infiltrative glioblastoma cells based on their distinctive morphological features in fresh mouse and human specimens [25].

A broadband CARS technique has been developed that uses greater spectral breadth within the fingerprint region of the Raman spectra without compromising imaging speed or sensitivity (Fig. 2) [26]. The biologically relevant Raman window ($500\text{--}3500\text{ cm}^{-1}$) was used to image a xenograft glioblastoma mouse model at high resolution ($< 10\ \mu\text{m}$). Pseudocolor three-channel broadband CARS microscopy was able to identify interfaces between xenograft brain tumors and the surrounding healthy brain matter.

Stimulated Raman histology

SRS microscopy has several advantages compared to CARS: superior nuclear contrast, linear relationship between signal intensity and chemical concentration, and a nondistorted spectrum nearly identical to spontaneous Raman scattering. Freudiger et al. published a landmark paper establishing SRS microscopy as a new method for label-free biomedical imaging in 2008 [27]. Subsequent innovations enhanced the collection of the backscattered signal and increased the imaging speed by three orders of magnitude to video rate, allowing for label-free *in vivo* imaging of biological tissues and the potential for clinical translation [28].

The use of SRS microscopy for differentiating healthy human and mouse brain tissue from tumor-infiltrated brain, both *ex vivo* and *in vivo*, based on histoarchitectural and biochemical differences was described in 2013 [29]. Two-channel SRS microscopy at 2845 cm^{-1} wavenumber (CH_2 /lipid channel) and 2930 cm^{-1} wavenumber (CH_3 /protein channel) is well suited for brain imaging by providing contrast between lipid-rich myelinated white matter and protein-rich nuclei [30]. During a simulated tumor resection using a xenograft mouse model, SRS microscopy was able to reveal tumor margins that were undetectable under standard operating conditions. In order to quantify the extent of brain tumor infiltration, a classifier system based on three SRS image features: tissue cellularity, axonal density, and protein/lipid ratio was developed [31]. The SRS classifier was able to detect tumor infiltration with 97.5% sensitivity and 98.5% specificity. Quantitative SRS microscopy detected tumor infiltration in grossly normal brain, providing evidence that

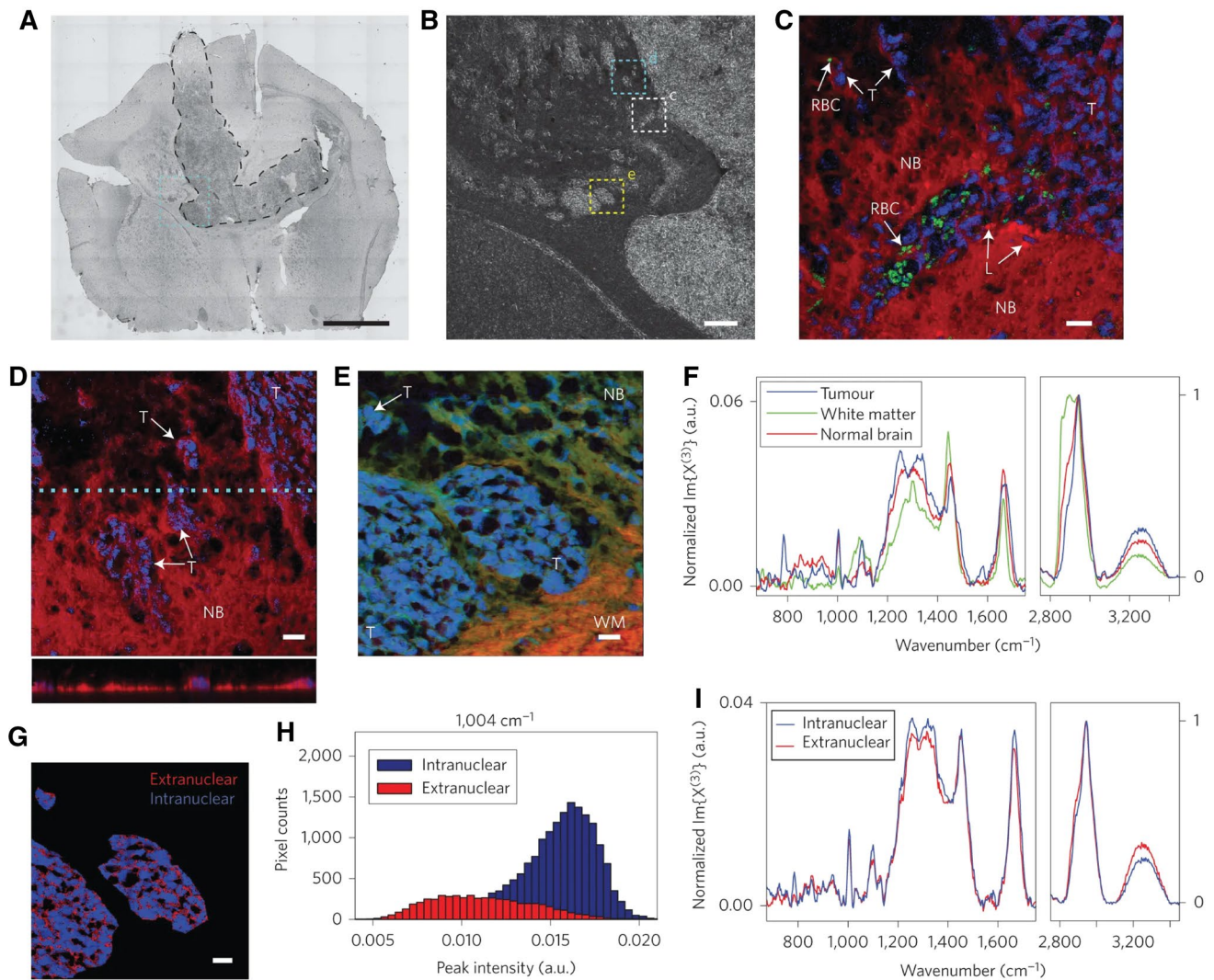


Fig. 2 Histopathology of glioma using broadband CARS. **a** Bright-field image of xenograft glioblastoma in mouse brain, with the tumor hard boundary outlined (black, dashed line). The cyan dashed box indicates a region of interest (ROI). Scale bar, 2 mm. **b** Phase contrast micrograph of broadband CARS region of interest with boxes and associated subfigure labels. Scale bar, 200 μm . **c** Pseudocolour broadband CARS image of tumor and normal brain tissue, with nuclei highlighted in blue, lipid content in red and red blood cells in green. **d** Broadband CARS image and axial scan with nuclei high-

lighted in blue and lipid content in red. **e** Broadband CARS image with nuclei highlighted in blue, lipid content in red and CH_3 stretch- CH_2 stretch in green. **NB** normal brain, **T** tumour cells, **RBC** red blood cells, **L** lipid bodies, **WM** white matter. **f** Single-pixel spectra. **g** Spectrally segmented image of intranuclear (blue) and extranuclear (red) tumoural spaces. **h** Histogram analysis of phenylalanine content. **i** Mean spectra from within a tumour mass. **c–e, g**, Scale bars, 20 μm . Figure and Caption adapted from Fig. 4 from [26]

this technique could improve tumor detection during brain tumor surgery.

Leveraging breakthroughs in fiber-laser-based technology [32], a clinical SRS microscope has been engineered and deployed in operating rooms across the US [8, 33]. Current intraoperative H&E histology is time-, labor-, and resource-intensive [34, 35]. To facilitate intraoperative interpretation of SRS images, we developed a method called stimulated Raman histology (SRH) (Fig. 3). To acquire an SRH image, a fresh, unprocessed surgical specimen is passed off the operative field and a small sample

(e.g. 3 mm^3) is compressed into a custom microscope slide. SRH images are acquired at the bedside and imaging time is approximately 90–120 s to acquire a 2×2 mm image. SRH is most useful for rapid diagnosis and tumor detection in surgical specimens. SRH combines SRS images and a virtual H&E image similar to standard intraoperative pathology and reveals the key diagnostic features of human brain tumor specimens (Fig. 4). In a simulation of intraoperative pathologic consultation in 30 patients, we found near-perfect concordance of SRH and conventional

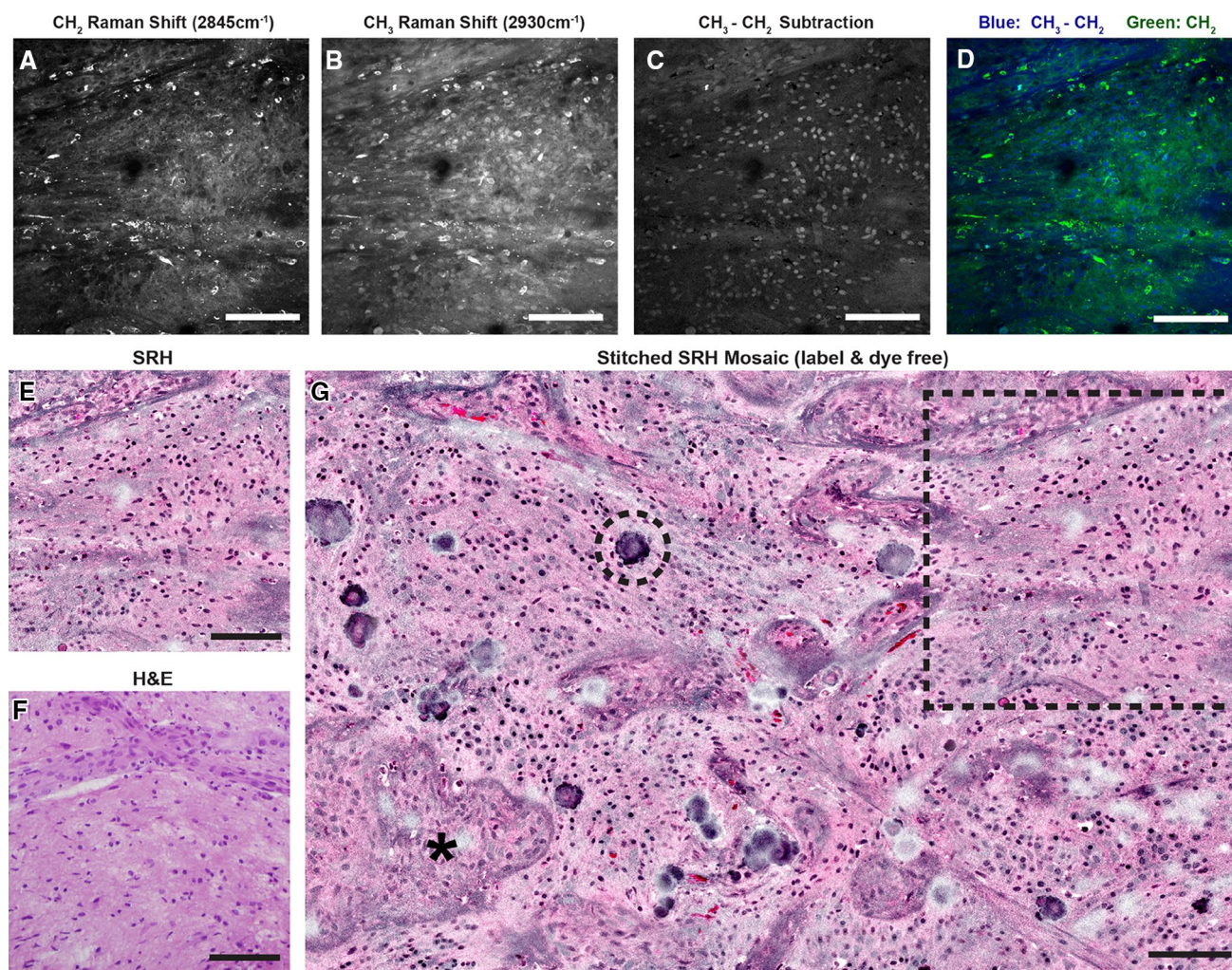


Fig. 3 Creating virtual H&E slides with the clinical SRS microscope. **a** $2845\text{ cm}^{-1}/\text{CH}_2$ and **b** $2930\text{ cm}^{-1}/\text{CH}_3$ images are acquired and **c** subtracted. **d** The CH_2 image is assigned to the green channel, and $\text{CH}_3\text{-CH}_2$ image is assigned to the blue channel to create a two-color blue-green image. Applying a virtual H&E color scheme, SRH images **e** are comparable to a similar section of tumor **f** imaged

after formalin-fixation, paraffin-embedding (FFPE), and H&E staining. **g** Mosaic tiled image of several SRH FOVs to create a mosaic of imaged tissue. Asterisk (*) indicates a focus of microvascular proliferation, dashed circle indicates calcification, and the dashed box demonstrates how the FOV in **e** fits into the larger mosaic. Scale bars = $100\text{ }\mu\text{m}$. Figure and Caption adapted from Fig. 2 from [8]

H&E histology for predicting diagnosis (Cohen's kappa, $\kappa > 0.89$), with an accuracy exceeding 92%.

Because SRH images are acquired digitally, they can be used to train and deploy computer vision systems for automated diagnosis. Our initial study used a neural network classifier, trained using histologic image features (e.g. cellularity, nuclear morphology, etc.), and was able to predict brain tumor subtype with 90% accuracy [8]. We then leveraged the recent developments in deep learning to train a convolutional neural network (CNN) on 2.6 million SRH images from over 500 patients to classify 13 of the most common histologic brain tumor subtypes (manuscript in preparation). We completed a randomized, prospective clinical trial (total patients, $N = 278$) comparing the accuracy of conventional H&E histology with board-certified

neuropathologist's diagnosis versus SRH plus CNN classification to validate our automated diagnostic pipeline. We found that SRH plus CNN was noninferior to conventional H&E histology, with an overall diagnostic accuracy of 94.6% versus 93.9%, respectively. The computer vision algorithm developed an "intelligence" for a hierarchy of recognizable histologic feature representations to classify the major histopathologic classes of brain tumors. The CNN was able to detect lipid-rich axons, nuclear and cellular morphology, lipid droplets commonly seen in necrotic tumors, and various chromatin structures. The findings of the prospective trial demonstrate how SRH can improve the care of brain tumor patients by making histologic information available to guide decision-making during surgery.

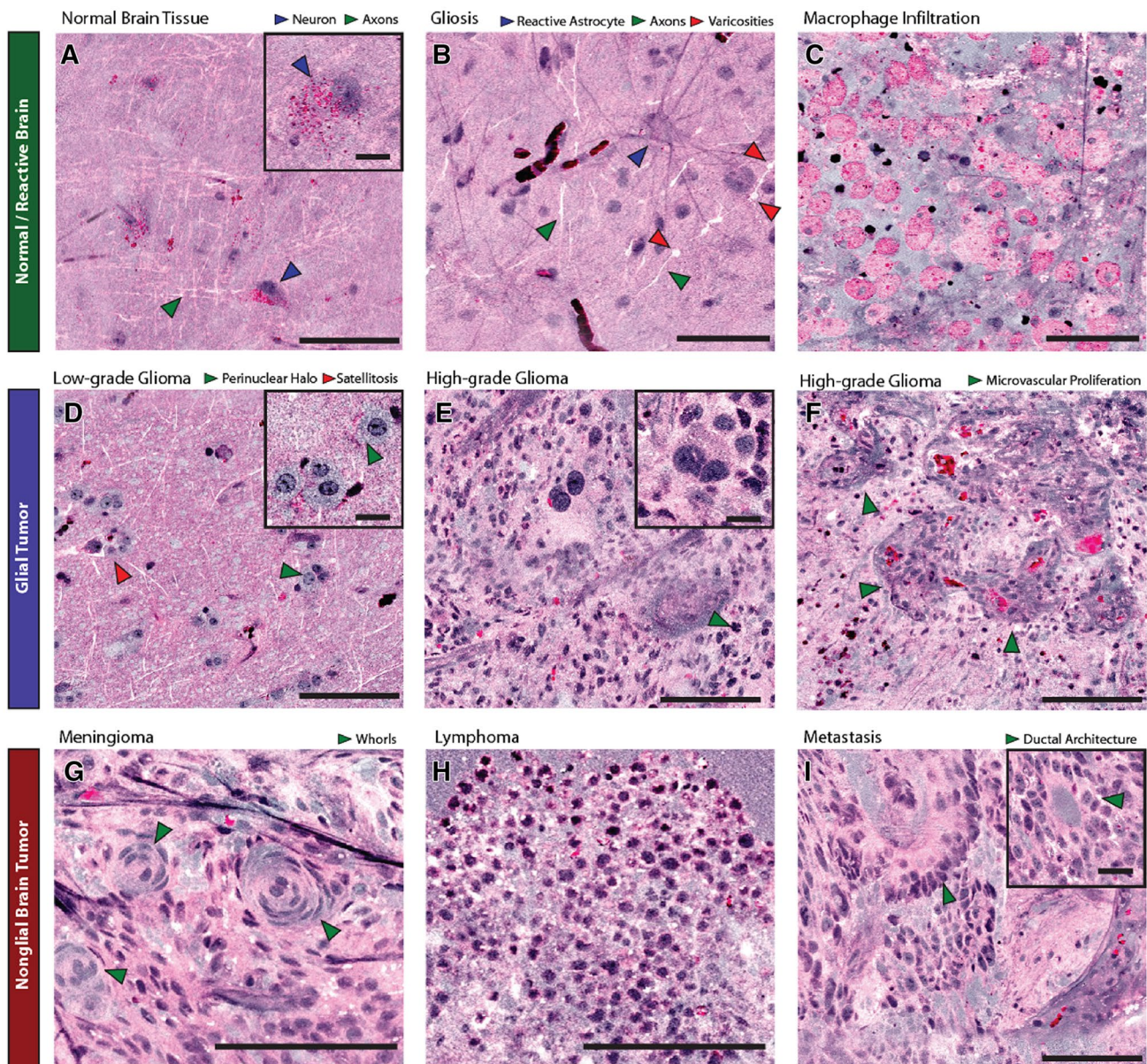


Fig. 4 Imaging key diagnostic histoarchitectural features with SRH. **a** Normal cortex reveals scattered pyramidal neurons (blue arrowheads) with angulated boundaries and lipofuscin granules, which appear red. White linear structures are axons (green arrowheads). **b** Gliotic tissue contains reactive astrocytes with radially directed fine protein-rich processes (red arrowheads) and axons (green arrowheads). **c** A macrophage infiltrate near the edge of a glioblastoma reveals round, swollen cells with lipid-rich phagosomes. **d** SRH reveals scattered “fried-egg” tumor cells with round nuclei, ample cytoplasm, perinuclear halos (yellow arrowheads), and neuronal satellitosis (purple arrowhead) in a diffuse 1p19q-co-deleted low-grade oligodendroglioma. Axons (green arrowhead) are apparent in this tumor-infiltrated cor-

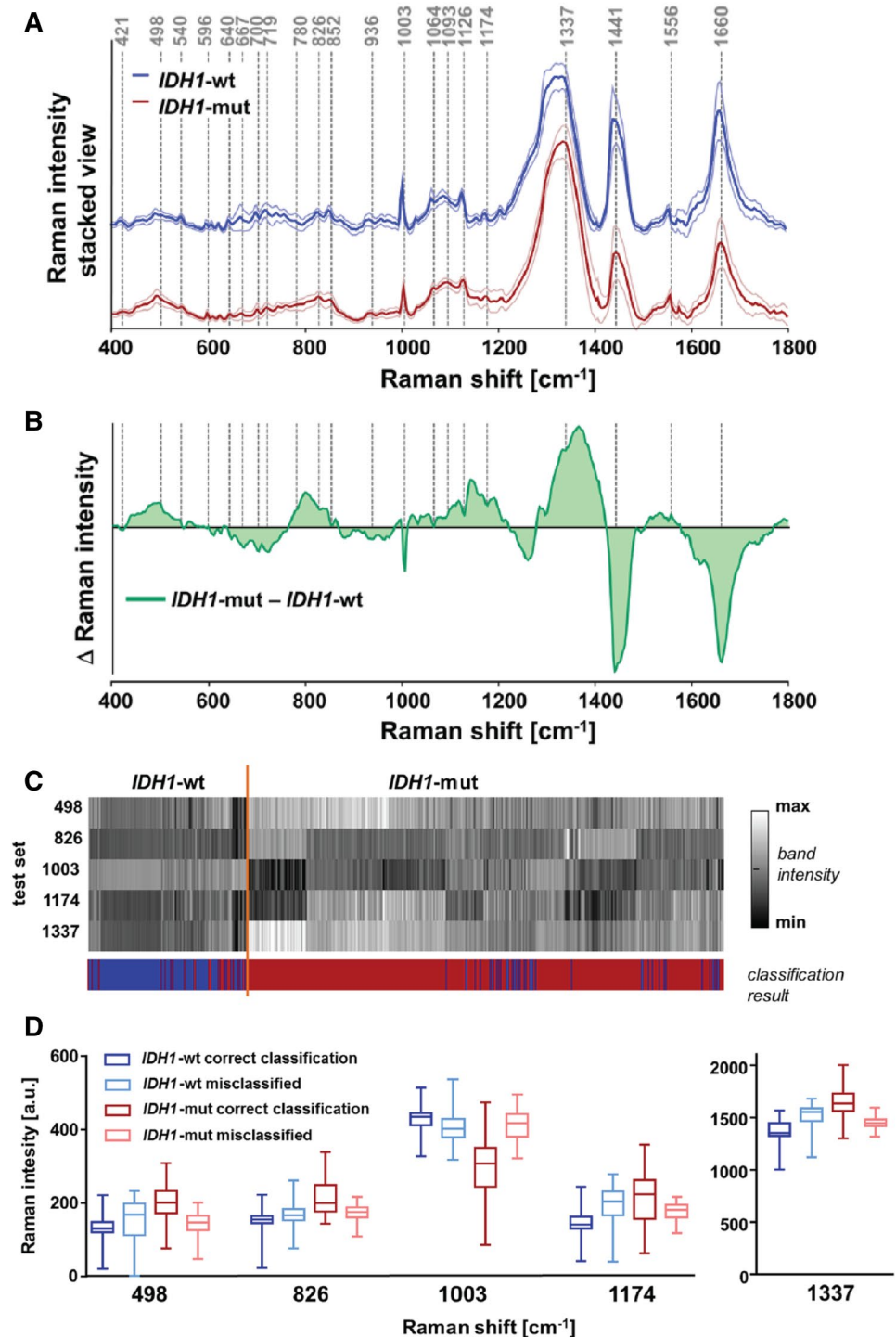
tex as well. **e** SRH demonstrates hypercellularity, anaplasia, and cellular and nuclear pleomorphism in a glioblastoma. A large binucleated tumor cell is shown (inset) in contrast to smaller adjacent tumor cells. **f** SRH of another glioblastoma reveals microvascular proliferation (orange arrowheads) with protein-rich basement membranes of angiogenic vasculature appearing purple. **g** SRH reveals the whorled architecture of meningioma (black arrowheads), **h** monomorphic cells of lymphoma with high nuclear:cytoplasmic ratio, and **i** the glandular architecture (inset; gray arrowhead) of a metastatic colorectal adenocarcinoma. Large image scale bars = 100 μm ; inset image scale bars = 20 μm . Figure and Caption adapted from Fig. 3 from [8]

Beyond histopathology

The majority of Raman-based imaging techniques have been applied to identifying histologic or histopathologic entities,

such as normal brain, edematous white matter, necrosis, and brain tumor classes. However, a major advantage of vibrational microscopy over standard light microscopy is the label-free contrast mechanisms due to characteristic

Fig. 5 Classification of IDH-wt and IDH-mut human gliomas using Raman spectroscopy. **a** Comparison of Raman spectra of IDH1-wt and IDH1-mut gliomas. Mean spectra with standard deviation of brain tumors with IDH1 wild type (blue curve, $n=12$) and with IDH1 mutation (red curve, $n=24$). **b** The difference spectrum is shown (IDH-mut minus IDH-wt). Dashed lines indicate characteristic Raman bands of brain tumors. **c** The Raman band intensities at 498, 826, 1003, 1174 and 1337 cm^{-1} are shown for each spectrum of the test set (in grayscale, min–max normalization for each band). Those were used for classification based on Mahalanobis distances. The result of the classification is shown in a color code: Blue represents IDH1-wt and red represents IDH1-mut. **d** The selected Raman band intensities are plotted separately for correctly classified and misclassified spectra with IDH1-wt and IDH1-mut genotype, respectively. Box and whiskers show 25–75% and 1–99% percentile, respectively. The median is indicated. Figure and Caption adapted from Figs. 1 and 3 from [9]



frequencies of various chemical bonds and the intrinsic biomolecular properties of the tissue. In addition to morphologic imaging, CRS microscopy provides high-sensitivity molecular imaging that can be used to obtain metabolomic, pharmacologic, and genetic information of biomedical specimens [36–40].

Zhou et al. used visible resonance Raman spectroscopy to identify the molecular vibrational fingerprints of carotenoids, tryptophan, amide I/II/III, proteins, and lipids as in situ spectral biomarkers to differentiate glioma grades (lower grade and malignant gliomas) [41]. By using Raman spectral peaks correspond main vibrational modes of specific compounds, a support vector machine classifier was

able to diagnosis normal brain, low grade glioma (WHO grade I and II), and malignant gliomas (WHO grade III and IV) with a total accuracy of 75%.

Recent studies have moved beyond the traditional WHO glioma grading criteria towards molecular diagnostics [9, 42, 43]. Mutations in isocitrate dehydrogenase (IDH) are the most important for stratifying patient outcomes using the molecular classification of gliomas [44, 45]. One study used Raman spectroscopy to classify glioma cryosections into IDH1-wildtype and IDH1-mutant tumors (Fig. 5) [9]. Raman spectral analysis demonstrated increased band intensities related to DNA in IDH1 mutant gliomas while bands assigned to molecular vibrations of lipids were significantly decreased. Intensities of Raman bands assigned to proteins differed in IDH1 mutant and IDH1 wild-type glioma, suggesting alterations in the protein profile. Five Raman spectral bands (498, 826, 1003, 1174 and 1337 cm^{-1}) were used to classify the IDH1 genotype of 36 frozen sectioned gliomas with an accuracy 89%. Livermore et al. performed a similar investigation on fresh intraoperative specimens, classifying three different glioma genetic subtypes: astrocytoma, IDH-wildtype; astrocytoma, IDH-mutant; oligodendroglioma, IDH-mutant, 1p19q co-deleted [42]. For predicting IDH mutational status alone, the trained classifier (PCA with linear discriminant analysis) was able to achieve a sensitivity of 91% and a specificity of 95%. The classifier demonstrated 79–94% sensitivity and 90–100% specificity for predicting the 3 glioma genetic subtypes. The process from tissue acquisition to genetic classification takes under 15 min.

Conclusion

Raman-based imaging methods can provide label-free histologic and chemical data in the operating room without the need for labels or dyes. Preclinical evidence suggests that Raman spectroscopy and CARS have value in the detection of brain tumors. If their use can be validated and adapted for clinical use, it is possible that handheld Raman spectroscopy probes could detect in situ brain tumor infiltration. SRH, the only FDA-registered Raman-based method available today, can be used alone or in combination with automated neural network-based classifiers to supplement the practice of intraoperative brain tumor diagnosis. Preliminary data indicate that Raman-based methods may hold promise in the classification of the genetic subtypes of malignant and lower grade gliomas by detecting specific mutations (e.g. IDH-1). Ultimately, the major advantage of label-free Raman-based methods is the ability to generate user-defined imaging data with rapid feedback to inform clinical decisions and improve the neurosurgical care of brain tumor patients.

Compliance with ethical standards

Conflict of interest Dr. Orringer is a shareholder in Invenio Imaging, Inc.

Ethical approval This article does not contain any studies with human participants or animals performed by any of the authors.

References

1. Senft C, Bink A, Franz K et al (2011) Intraoperative MRI guidance and extent of resection in glioma surgery: a randomised, controlled trial. *Lancet Oncol* 12:997–1003
2. Hollon T, Hervey-Jumper SL, Sagher O, Orringer DA (2015) Advances in the surgical management of low-grade glioma. *Semin Radiat Oncol* 25:181–188
3. Stummer W, Pichlmeier U, Meinel T et al (2006) Fluorescence-guided surgery with 5-aminolevulinic acid for resection of malignant glioma: a randomised controlled multicentre phase III trial. *Lancet Oncol* 7:392–401
4. Lau D, Hervey-Jumper SL, Chang S et al (2016) A prospective Phase II clinical trial of 5-aminolevulinic acid to assess the correlation of intraoperative fluorescence intensity and degree of histologic cellularity during resection of high-grade gliomas. *J Neurosurg* 124:1300–1309
5. Hollon T, Lewis S, Freudiger CW et al (2016) Improving the accuracy of brain tumor surgery via Raman-based technology. *Neurosurg Focus* 40:E9
6. Kalkanis SN, Kast RE, Rosenblum ML et al (2014) Raman spectroscopy to distinguish grey matter, necrosis, and glioblastoma multiforme in frozen tissue sections. *J Neurooncol* 116:477–485
7. Jermyn M, Mok K, Mercier J et al (2015) Intraoperative brain cancer detection with Raman spectroscopy in humans. *Sci Transl Med* 7:274ra19
8. Orringer DA, Pandian B, Niknafs YS et al (2017) Rapid intraoperative histology of unprocessed surgical specimens via fibre-laser-based stimulated Raman scattering microscopy. *Nat Biomed Eng*. <https://doi.org/10.1038/s41551-016-0027>
9. Uckermann O, Yao W, Juratli TA et al (2018) IDH1 mutation in human glioma induces chemical alterations that are amenable to optical Raman spectroscopy. *J Neurooncol* 139:261–268
10. Raman CV, Krishnan KS (1928) A new type of secondary radiation. *Nature* 121:501–502
11. Tashibu K (1990) Analysis of water content in rat brain using Raman spectroscopy. *No To Shinkei* 42:999–1004
12. Krafft C, Neudert L, Simat T, Salzer R (2005) Near infrared Raman spectra of human brain lipids. *Spectrochim Acta A Mol Biomol Spectrosc* 61:1529–1535
13. Köhler M, Machill S, Salzer R, Krafft C (2009) Characterization of lipid extracts from brain tissue and tumors using Raman spectroscopy and mass spectrometry. *Anal Bioanal Chem* 393:1513–1520
14. Kirsch M, Schackert G, Salzer R, Krafft C (2010) Raman spectroscopic imaging for in vivo detection of cerebral brain metastases. *Anal Bioanal Chem* 398:1707–1713
15. Koljenović S, Choo-Smith L-P, Bakker Schut TC et al (2002) Discriminating vital tumor from necrotic tissue in human glioblastoma tissue samples by Raman spectroscopy. *Lab Invest* 82:1265–1277
16. Kast RE, Auner GW, Rosenblum ML et al (2014) Raman molecular imaging of brain frozen tissue sections. *J Neurooncol* 120:55–62

17. Kast R, Auner G, Yurgelevic S et al (2015) Identification of regions of normal grey matter and white matter from pathologic glioblastoma and necrosis in frozen sections using Raman imaging. *J Neurooncol* 125:287–295
18. Desroches J, Jermyn M, Mok K et al (2015) Characterization of a Raman spectroscopy probe system for intraoperative brain tissue classification. *Biomed Opt Express* 6:2380–2397
19. Jermyn M, Desroches J, Mercier J et al (2016) Neural networks improve brain cancer detection with Raman spectroscopy in the presence of operating room light artifacts. *J Biomed Opt* 21:94002
20. Jermyn M, Desroches J, Mercier J et al (2016) Raman spectroscopy detects distant invasive brain cancer cells centimeters beyond MRI capability in humans. *Biomed Opt Express* 7:5129–5137
21. Jermyn M, Mercier J, Aubertin K et al (2017) Highly accurate detection of cancer in situ with intraoperative, label-free, multimodal optical spectroscopy. *Cancer Res* 77:3942–3950
22. Evans CL, Xu X, Kesari S et al (2007) Chemically-selective imaging of brain structures with CARS microscopy. *Opt Express* 15:12076–12087
23. Evans CL, Xie XS (2008) Coherent anti-stokes Raman scattering microscopy: chemical imaging for biology and medicine. *Annu Rev Anal Chem* 1:883–909
24. Uckermann O, Galli R, Tamosaityte S et al (2014) Label-free delineation of brain tumors by coherent anti-stokes Raman scattering microscopy in an orthotopic mouse model and human glioblastoma. *PLoS ONE* 9:e107115
25. Galli R, Uckermann O, Temme A et al (2017) Assessing the efficacy of coherent anti-stokes Raman scattering microscopy for the detection of infiltrating glioblastoma in fresh brain samples. *J Biophotonics* 10:404–414
26. Camp CH Jr, Lee YJ, Heddleston JM et al (2014) High-speed coherent Raman fingerprint imaging of biological tissues. *Nat Photonics* 8:627–634
27. Freudiger CW, Min W, Saar BG et al (2008) Label-free biomedical imaging with high sensitivity by stimulated Raman scattering microscopy. *Science* 322:1857–1861
28. Saar BG, Freudiger CW, Reichman J et al (2010) Video-rate molecular imaging in vivo with stimulated Raman scattering. *Science* 330:1368–1370
29. Ji M, Orringer DA, Freudiger CW et al (2013) Rapid, label-free detection of brain tumors with stimulated Raman scattering microscopy. *Sci Transl Med* 5:201ra119
30. Lu F-K, Calligaris D, Olubiyi OI et al (2016) Label-free neurosurgical pathology with stimulated Raman imaging. *Cancer Res* 76:3451–3462
31. Ji M, Lewis S, Camelo-Piragua S et al (2015) Detection of human brain tumor infiltration with quantitative stimulated Raman scattering microscopy. *Sci Transl Med* 7:309ra163
32. Freudiger CW, Yang W, Holtom GR et al (2014) Stimulated Raman scattering microscopy with a robust fibre laser source. *Nat Photonics* 8:153–159
33. Hollon TC, Lewis S, Pandian B et al (2018) Rapid intraoperative diagnosis of pediatric brain tumors using stimulated Raman histology. *Cancer Res* 78:278–289
34. Mahe E, Ara S, Bishara M et al (2013) Intraoperative pathology consultation: error, cause and impact. *Can J Surg* 56:E13–E18
35. Somerset HL, Kleinschmidt-DeMasters BK (2011) Approach to the intraoperative consultation for neurosurgical specimens. *Adv Anat Pathol* 18:446–449
36. Anna I, Bartosz P, Lech P, Halina A (2017) Novel strategies of Raman imaging for brain tumor research. *Oncotarget* 8:85290–85310
37. Shi L, Zheng C, Shen Y et al (2018) Optical imaging of metabolic dynamics in animals. *Nat Commun* 9:2995
38. Hu F, Lamprecht MR, Wei L et al (2016) Bioorthogonal chemical imaging of metabolic activities in live mammalian hippocampal tissues with stimulated Raman scattering. *Sci Rep* 6:39660
39. Fu D, Zhou J, Zhu WS et al (2014) Imaging the intracellular distribution of tyrosine kinase inhibitors in living cells with quantitative hyperspectral stimulated Raman scattering. *Nat Chem* 6:614–622
40. Hollon TC, Orringer DA (2018) Shedding light on IDH1 mutation in gliomas. *Clin Cancer Res* 24:2467–2469
41. Zhou Y, Liu C-H, Wu B et al (2019) Optical biopsy identification and grading of gliomas using label-free visible resonance Raman spectroscopy. *J Biomed Opt* 24:1–12
42. Livermore LJ, Isabelle M, Bell IM et al (2019) Rapid intraoperative molecular genetic classification of gliomas using Raman spectroscopy. *Neuro Oncol Adv*. <https://doi.org/10.1093/oaajnl/vdz008>
43. Uckermann O, Juratli TA, Galli R et al (2018) Optical Analysis of glioma: fourier-transform infrared spectroscopy reveals the IDH1 mutation status. *Clin Cancer Res* 24:2530–2538
44. Cancer Genome Atlas Research Network, Brat DJ, Verhaak RGW et al (2015) Comprehensive, integrative genomic analysis of diffuse lower-grade gliomas. *N Engl J Med* 372:2481–2498
45. Louis DN, Perry A, Reifenberger G et al (2016) The 2016 World Health Organization classification of tumors of the central nervous system: a summary. *Acta Neuropathol* 131:803–820

Publisher's Note Springer Nature remains neutral with regard to jurisdictional claims in published maps and institutional affiliations.